Stabilization of Low-NOx Hydrogen Flames on a Dual-Swirl Coaxial Injector

Maxime Leroy, Clément Mirat, Antoine Renaud, Ronan Vicquelin

STABILIZATION OF LOW-NOX HYDROGEN FLAMES ON A DUAL-SWIRL COAXIAL INJECTOR

Maxime Leroy[*†]
Université Paris-Saclay, CNRS,
CentraleSupélec, EM2C Laboratory
8-10 rue Joliot-Curie, 91190 Gif-sur-Yvette, France
Email: maxime.leroy@centralesupelec.fr

Clément Mirat
Université Paris-Saclay, CNRS,
CentraleSupélec, EM2C Laboratory
8-10 rue Joliot-Curie, 91190 Gif-sur-Yvette, France

Antoine Renaud
Université Paris-Saclay, CNRS,
CentraleSupélec, EM2C Laboratory
8-10 rue Joliot-Curie, 91190 Gif-sur-Yvette, France

Ronan Vicquelin
Université Paris-Saclay, CNRS,
CentraleSupélec, EM2C Laboratory
8-10 rue Joliot-Curie, 91190 Gif-sur-Yvette, France

ABSTRACT

Hydrogen-fueled carbon-free energy is a growing prospect for the future of several industries, including the aeronautical and energy generation sectors. However, the transition to hydrogen comes with several challenges: flame stabilization due to the unique combustion properties of hydrogen compared to conventional fuels and control of nitrogen oxides (NO_x) production due to the higher combustion temperature. In addition, the high flammability of hydrogen poses an increased risk of flashback in premixed configurations commonly used to generate low-NO_x flames. As a consequence, research into strategies for low-NO_x hydrogen combustion is developing, and several technologies are being considered for industrial use. Among these technologies, we consider here a dual swirl coaxial injector operated in non-premixed conditions. This setup enables the stabilization of multiple types of flame structures that are parametrically investigated for their NO_x emissions. The flame structure is observed using OH* chemiluminescence images collected using an intensified CCD camera equipped with a band-pass filter. Exhaust gas species mole fractions of NO, NO_2 and O_2 are measured using NDIR gas detectors and a paramagnetic sensor. This investigation reveals that stabilization of hydrogen-air flames on the double swirl injector is possible and that varying the flow parameters induces changes in structure that affect NO_x emissions, independently of swirl level, residence time, and temperature that also play a role. The study is carried out at atmospheric pressure.

[*]Address all correspondence to this author
[†]This author is now employed by Safran SA

NOMENCLATURE

Variables

$_1$	Subscript for central (fuel) channel
$_2$	Subscript for annular (air) channel
d	Channel diameter [mm]
e	Inner channel lip thickness [mm]
G_θ	Axial flux of azimuthal momentum [N]
G_z	Axial flux of axial momentum [N·m]
J	Momentum flux ratio [-]
$\dot{m}$	Channel mass flow rate [kg·s^{-1}]
$\mathscr{P}_{th}$	Flame thermal power [kW]
Re	Reynolds number Re$= \frac{dU}{\nu}$ [-]
ρ	Density [kg·m^{-3}]
S	Swirl number [-]
τ_{res}	Estimated mean residence time in the chamber [s]
V	Combustion chamber volume [m^3]
U	Channel bulk velocity [m·s^{-1}]

Abbreviations

CRZ	Central Recirculation Zone
NO_x	Nitrogen oxides NO and NO_2
OH*	Excited OH radical

1 INTRODUCTION

To mitigate climate change, carbon-free combustion can be a game-changing technology for many industrial processes as well as air transportation. One way to reach this objective is through the use of hydrogen as fuel, as long as its production is carbon-free. However, the combustion of hydrogen may often produce harmful nitrogen oxides (NO_x). NO_x are of particular concern as they have adverse effects on human health [1], the environment, and participate in climate change, especially when emitted at high altitudes [2]. Thus, technologies have to be developed that allow low-NO_x hydrogen combustion. In hydrogen combustion, a great part of NO_x are generated through the thermal or Zeldovich pathway [3] that occurs when high flame temperatures are reached, therefore a focus is placed on the control of temperature within the chamber. Several techniques have been developed and studied to achieve this control, like modifying the mixture composition through steam or exhaust gas injection [4, 5], by staging combustion [6, 7] or by enhancing

mixing before or after the injector [8–10]. Swirled flames have already proven their efficiency under gas turbine conditions for lean premixed configurations [11, 12] and ways to reduce flashback have been studied experimentally [13, 14] and numerically [15].

In this paper, non-premixed swirled combustion is used to generate a flame and control NO_x emissions. Swirled flows are known to stabilize flames and are widely used in gas turbines to achieve stable combustion. They can limit flame blow-out [16], especially in the case of non-premixed hydrogen combustion [17], and recirculation zones created by swirl help with flame stabilization [18]. Using a non-premixed configuration also avoids flashback which is often problematic in hydrogen flames. However, the reduced mixing efficiency of non-premixed systems can result in higher NO_x emissions [19], which makes studies on non-premixed hydrogen flames rare. Swirl flows also affect flame structure and NO_x emissions [20]. These properties have driven the development of the Oxytec dual-swirl coaxial injector considered in this work. This particular configuration adds a degree of control over the flow as opposed to the standard practice of swirling only the outer flow. This has allowed Degenève et al. [21, 22] to uncover diverse flame structures dependent on swirl with oxygen-enriched flames (or oxyflames) on this injector. However, pollutant emissions from the stabilized flames were not characterized. Moreover, Merlo et al. [23] have shown that swirl could decrease NO_x emissions in oxygen-enhanced combustion. These works suggest that a similar effect could be found in hydrogen flames as both methane oxyflames and hydrogen flames possess high reactivity and high flame temperatures. Thus, an experiment using the Oxytec injector and hydrogen fuel was developed to study the evolution of NO_x emissions in a non-premixed configuration under the variation of the available injection parameters. The aim of this work is then to ascertain whether low NO_x emissions can be achieved on a swirling coaxial injector and show how the various injection parameters control the behavior of the flame structure and the associated nitrogen oxides emissions.

This paper is divided into three parts. In the first part, the combustion chamber and injector are described, along with the different diagnostics used on the experiment, as well as the different parameters that are varied during the experiment. In the second part, the various structures produced on the coaxial swirl injector are presented, as well as their evolution under the different injection parameters. Finally, the evolution of NO_x emissions of the hydrogen flames and the chamber exit temperature with varying swirl levels are exposed to analyze the behavior of NO_x production on this injector.

2 EXPERIMENTAL SETUP

This section presents the studied configuration (combustion chamber and injector), the controlling parameters and employed diagnostics.

Combustion chamber

The combustion chamber used in the experiments is shown in Fig. 1(a). This chamber is a rectangular cuboid of side length 150 mm and height 240 mm in which the injector described in [22] is placed. The operating pressure is atmospheric. The chamber dump

plane is water-cooled to avoid damaging the injector. The chamber is enclosed by four quartz windows to ensure accessibility for optical diagnostics. These windows constitute the walls of the chamber and are supported by four vertical hollow steel beams in the corners. Temperature measurements are made at two points in the chamber. One K-type thermocouple is placed within one of the hollow corner supports of the chamber to monitor wall temperatures. Chamber exhaust temperature is measured with two R-type thermocouples of radius 200 µm and 450 µm. The readings are then corrected using the Reduced radiative error method developed by Brohez et al. [24].

Injector

The injector used in this work is coaxial, with the central channel dedicated to fuel injection (in this case, hydrogen) and the annular channel for air injection, as described in Fig. 1(b). The inner channel has a diameter of $d_1 = 6$ mm and a lip of thickness $e = 1$ mm, while the annular channel has an external diameter of $d_2 = 20$ mm. The outlet of the channels is elevated 5 mm above the chamber dump plane to ensure good visibility of the flame root. Gas injection is managed using three Bronkhorst EL-FLOW mass flow controllers: hydrogen injection is controlled by a 12 Nm^3/h (air) flow controller, and axial and tangential air injections are each controlled by a 400 NL/min (air) flow controller. All flow meters have a 0.1% of full-scale stability and 0.2% repeatability.

This injector design allows for swirling flows in both the central and annular channels of injection. Swirl is imparted to the flow differently in each channel. The swirl number, defined as the ratio of axial flux of axial momentum and axial flux of tangential momentum $S = \frac{G_\theta}{RG_z}$ [25], is estimated under the hypothesis of solid body rotation. The central channel has a housing for removable swirl vanes of varying pitch θ. In our study, the injector was used either with no vane, or with either 30° or 60° vanes. The inner swirl number S_1 can then be expressed as:

$$S_1 = \frac{1}{2}\tan(\theta) \tag{1}$$

The flow in the annular channel is swirled with an axial-tangential swirler. Varying the mass flow rate in the axial and tangential channels changes the swirl number according to the formula:

$$S_2 = \frac{S_{2,max}}{1 + \frac{Q_{2,z}}{Q_{2,\theta}}} \tag{2}$$

where $S_{2,max} = 1.23$ is the maximum swirl number associated with the swirler geometry (see [21]) and $Q_{2,\theta}$ and $Q_{2,z}$ are respectively the axial and tangential volumetric flow rates in the annular channel.

The flames produced can then be modified thanks to four injection parameters: the fuel mass flow rate $\dot{m}_1$, the axial air mass flow

rate, the tangential air mass flow rate and the inner swirl vane. The total air mass flow rate is denoted $\dot{m}_2$. In this study, the fuel mass flow rate sets the flame thermal power $\mathscr{P}_{th}$. Changes in the other injection parameters then allow the variation of three non-dimensional flow parameters that we use to define our flames: S_1, S_2 and J. The inner channel swirl number S_1 depends directly on the swirl vane angle. Contrary to the other flame parameters, S_1 cannot be changed continuously and at the same time as the other parameters as it is tied to a part of the injector. The outer channel swirl number S_2 depends on the axial to tangential air injection ratio as described in equation 2. Finally, the momentum flux ratio J depends on the ratio of fuel mass flow rate to total air mass flow rate. Incidentally, this ratio also defines the global equivalence ratio Φ of the flame:

$$J = \frac{\rho_2 {U_2}^2}{\rho_1 {U_1}^2} = \frac{A_1^2 \rho_1}{A_2^2 \rho_2} \frac{\dot{m}_2^2}{\dot{m}_1^2} \quad \text{and} \quad \Phi = s \frac{\dot{m}_1}{Y_{2,O_2} \dot{m}_2}, \tag{3}$$

with s = 8, the mass stoichiometric ratio and Y_{2,O_2} = 0.233 the oxygen mass fraction in the oxidizer stream . Thus:

$$\Phi = \sqrt{\frac{\rho_1}{\rho_2}} \frac{s A_1}{Y_{2,O_2} A_2 \sqrt{J}} = \frac{0.971}{\sqrt{J}} \tag{4}$$

This relationship is plotted in Fig. 2. It is apparent that above $J = 15$, variations in momentum flux ratio cause very little variation in equivalence ratio, but a strong variation is observed between $J = 0$ and $J = 5$ with an intermediate region of slower variation between $J = 5$ and $J = 15$. Considering this link between global equivalence ratio and momentum flux ratio, the metric $J^{-\frac{1}{2}}$ is employed in the following work. The effect this change of equivalence ratio has on adiabatic flame temperature is also plotted in Fig. 2.

Hydrogen flames are generated for three different values of S_1: 0, 0.29 and 0.87. For each value of S_1, the parameters S_2 and J are varied. S_2 is varied by increments of 0.1 from 0.6 to 0.8 and is co-rotating with S_1. To explore a large range of values for J, the variation is made according to the metric $J^{-\frac{1}{2}}$, by increments of 0.1 from 0.2 to 0.9. However, the points at $J^{-\frac{1}{2}} = 0.2$ and $S_2 = 0.8$ cannot be achieved as this configuration exceeds the maximum flow rate allowed by our flow meters. Experimentation with the flame parameters has shown hysteresis, where flame structures are dependent on the path of S_2 and J leading to the operating point. Thus, a choice is made as to the order in which these parameters were varied, with priority given to the variation of momentum ratio J. As a result, the full range of J is explored before modifying the value of S_2. The different variations in parameters are summarized in Table 1. One can see from the values presented within that table that the flow in the annular channel is well into the turbulent regime with a Reynolds number above 7000. Due to the low kinematic viscosity of hydrogen, the Reynolds number in the inner channel stands at the entrance of the transition region at 2000, but increasing bulk velocity (see Effect of thermal power) has not revealed any transitions in the flow

visible in our flame visualization.

Diagnostics

Flame structure is observed using OH* chemiluminescence. A Princeton Instruments PI-MAX4 ICCD camera is equipped with a NIKKOR 105mm UV objective and an Asahi SPECTRA XBPA310 310 $\pm$ 5 nm bandpass filter. Aperture is fixed at f/8.0 and the minimum exposure time is $\Delta t = 10$ ms. To construct the mean images, 15 images are composed together. Afterwards, the images are post-processed by inverse Abel transform to visualize the flame front, and a Gaussian filter is applied to lessen the noise induced by this transform.

Exhaust gases composition analysis is performed using a HORIBA VA-5111 multi-component gas analyzer unit associated with a VS-5000 series sampling unit. This enables measurement of the molar fraction of the species of interest: O_2, measured using a paramagnetic sensor, and NO measured using a NDIR sensor. Prior to being analyzed, the exhaust gases are dried through a condenser. Measurement of total NO_x (NO+ NO_2) is obtained using a NO_2 to NO converter upstream of the analyzer unit that can be toggled by a switch. The manufacturer-specified errors for each sensors are presented in Table 2. The sensors are calibrated using calibration gas bottles with a 3% precision on composition.

To compensate for the variation in global equivalence ratio induced by the modification of the momentum flux ratio J, the measured emissions are corrected for oxygen level at 15% O_2 as described in Baukal and Eleazer [26].

$$NO_{\text{x, corrected}} = NO_{\text{x}} \frac{0.2095 - 0.15}{0.2095 - O_{2,\text{exhaust}}} \tag{5}$$

Gas molar fractions are measured once the chamber reaches thermal equilibrium, indicated by the stabilization of the wall temperature, to avoid possible transient effects.

3 FLAME STRUCTURE

Experiments on the present injector reveal that hydrogen flames can stabilize in a variety of forms, as illustrated in Fig. 3. In a dark room, the flame's weak visible emission is captured in these images and presents features consistent with [27]: a red emission from high-temperature H_2O and grey-bluish flame fronts associated with broadband visible emission. From this image, one can observe the flame topologies stabilized above the coaxial injector, like a primary flame attached to the injector lips separating fuel and oxidizer or a secondary flame front protruding towards the injector. These structures are very similar in nature to what was observed for oxygen-enriched methane flames on the same injector in [21]. As such, an analogous classification is employed, with an additional flame type (V) added to account for new structures, as illustrated in Fig. 4.

Type I flames possess a diffusion flame front attached to the lips of the central channel. Type II flames show in addition to that a secondary flame front protruding towards the injector, centered on the injector's axis of symmetry and linked with the presence of a central recirculation zone (CRZ) close to the injector. A noticeable reactive front between the recirculating burnt gases and the injected fuel is sometimes also observed in flame type I. In this case, however, the CRZ is stabilized further downstream, which does not yield a secondary flame front close to the injector as in type II flames. The disappearance of the primary flame front defines flame type III. Type IV occurs when the secondary flame front moves downstream and away from the injector's central axis, with a strong influence from the CRZ. Finally, the newly observed type V occurs when the secondary flame front moves downstream and takes an elongated shape positioned on the central axis of the injector. In this type, the CRZ appears to be weaker, as the flame visualization does not show a wide-angle flame front like in other structures where the presence of the CRZ is known. This would explain the position of the flame front directly along the central axis. Figure 3 is annotated to indicate the corresponding flame type. They share identical thermal powers and inner swirl number $S_1 = 0.87$. The flame shapes are modified by adapting J and S_2, whose values are displayed in each image.

To better identify the flame fronts and assess the flame topology, Fig. 5 presents the different half-images obtained by OH* chemiluminescence accompanied by an inverse Abel transform when exploring the $J - S_2$ space, with $S_1 = 0.87$ at fixed thermal power $\mathscr{P}_{th} = 10$ kW. It can be observed that detached flames (types IV and V) are more likely to appear at low outer swirl numbers S_2 and are not present when S_2 reaches 0.8. Conversely, attached flame types I and II only appear for the highest outer swirl number. Presumably, this could be caused by a link between the CRZ position and the outer swirl number, with the CRZ being brought towards the injector at high outer swirl levels and promoting flame attachment. This upstream movement of the CRZ at higher swirl levels can be explained by the larger swirl decay after the injector exit inducing a stronger adverse pressure gradient [28]. The other parameter, $J^{-\frac{1}{2}}$, appears to have an opposite effect, with a transition from a near attached flame (type III) to a fully detached flame occurring between $J^{-\frac{1}{2}} = 0.2$ and 0.3 for $S_2 = 0.7$. Likewise, the liftoff height of detached flames at $J^{-\frac{1}{2}} = 0.9$ appears higher than detached flame at lower values of $J^{-\frac{1}{2}}$, suggesting that increasing $J^{-\frac{1}{2}}$ moves the CRZ downstream, which would agree with the scaling law observed of the stagnation point in [29]. This movement of the CRZ could also explain the transition from type II to type I observed at $S_2 = 0.8$. No flame at $S_2 = 0.8$, $J^{-\frac{1}{2}} = 0.2$ could be produced due to the flow rate limits mentioned previously.

The other parameter of interest that was not explored in the previous figure is the inner swirl S_1. The evolution of S_1 can also have a significant effect on structure, as illustrated in Fig. 6. The increase in inner swirl level first brings the flame closer to the injector, by causing a transition from a long jet-like type I flame to a shorter, more compact flame. However, another effect of S_1 is to allow the stabilization of detached flames, as demonstrated by the presence of a type IV flame for $S_1 = 0.87$.

The modification of the control parameters, therefore, affects flow patterns and enables the generation of a wide variety of flame structures allowed by hydrogen's reactivity. As will be seen later, these various flame stabilization modes also have noticeable effects on NO_x emissions.

It was initially thought that the type V flame was a structure proper to hydrogen flames, as it had not been reported for methane

oxyflames in [21]. However, further investigation revealed that the flow conditions necessary for the apparition of type V flames were not met in that work, as they correspond to very low equivalence ratios not relevant in oxyflames where higher equivalence ratios are preferred to consume the added oxygen. Subsequent experiments showed that type V flames were indeed possible using this other oxidizer-fuel combination.

4 STUDY OF NO_x EMISSIONS

The emission of nitrogen oxides at the combustor outlet is studied for the different flames that can be stabilized by varying the injection control parameters.

Effect of thermal power

The thermal power in the chamber can be varied independently from the other flow parameters by scaling the injected mass flows by a common factor to conserve the momentum flux ratio. Consequently, the thermal power of a type I flame at $J^{-\frac{1}{2}} = 0.5$, $\Phi = 0.49$, $S_1 = 0.87$ and $S_2 = 0.8$ was varied between 5 and 15 kW, yielding the flames in Fig. 7. For the chosen conditions, it is apparent from the OH* images that flame structure remains here unchanged throughout the variation in thermal power, despite the increased flow rates. The flames are stabilized in a type I structure, with a primary flame attached at the lips of the central channel. The evolution of the NO_x emissions of these flames is monitored as well as the chamber exit temperature. In addition, as the evolution of thermal power modifies the total mass flow rate in the chamber, the ensuing change in residence time τ_{res} within the chamber is estimated. In the absence of detailed flow information, this estimation is performed with the formula $\tau_{res} = \frac{\rho_{exit} V}{\dot{m}}$, where V is the chamber volume, $\dot{m}$ is the total injected mass flow rate and ρ_{exit} is the estimated exit density. This density was obtained by computing the burned gas composition at equilibrium, and then setting the temperature of this mixture to the measured exit temperature. The results are presented in Table 3. It appears that increasing thermal power yields a decrease in measured NO_x emissions. It is also accompanied by a rise in exit temperature that suggests a higher temperature within the chamber. This should promote NO_x formation through the thermal pathway, whereas the opposite is observed. However, the estimated residence time also shows an significant decrease with increasing thermal power. It can then be explained that the lower residence time affects reaction kinetics to form fewer nitrogen oxides. As expected, along with the temperature, residence time participates in controlling NO_x production in the chamber. Further testing by varying residence time through the modification of chamber volume could be undertaken in future studies to bring additional information.

Effect of flame structure alone

The great variety of flame types obtained on the injector is achieved through variations of three parameters: inner and outer swirl, and momentum flux ratio. This can make the task of assigning the cause of the observed evolution in nitrogen oxide emissions difficult. However, since there is a hysteresis effect that takes place around transitions in structure, it is possible to stabilize two flame types under

the same injection parameters. It is important to note that, under thermalized conditions, these transitions are repeatable.

An example of this is illustrated in Fig. 8. During the exploration of the $J - S_2$ space undertaken in Fig. 5, the flame at $J^{-\frac{1}{2}} = 0.6$ and $S_2 = 0.7$ stabilizes under a type V structure. However, type IV structures appear when $J^{-\frac{1}{2}}$ increases above 0.7. By taking the inverse path and decreasing $J^{-\frac{1}{2}}$ back to 0.6 starting from a type IV flame, a type IV flame remains stabilized at $J^{-\frac{1}{2}} = 0.6$ and $S_2 = 0.7$. This allows a direct comparison between the emissions of the two structures exposed in Table 4. It appears that, under these conditions, the type IV structure releases NO_x levels nearly 5 ppm less than the type V structure. This change in NO_x emissions is also accompanied by a lower exit temperature measured in type IV flames. This behavior can be explained by the changes in flame shape observed between type IV and type V. In the type V flame, OH* chemiluminescence signal is present up to 100 mm above the injector, showing that combustion occurs within a wide volume of the chamber, whereas the OH* species is more localized along a single flame front in the type IV flame. The likely factor in the switching between type IV and V is the strength of the CRZ, which could provide enhanced mixing between fresh and burned gases and therefore lower the flame temperature and reduce the volume of high-temperature regions responsible for the production of thermal NO_x. In any case, it is apparent that flame structure plays a large role in the generation of nitrogen oxides independently from the variation in injection parameters.

Effect of the outer swirl number and momentum flux ratio

In addition to modifying the flame structure, swirl can have a direct effect on NO_x emissions. The modular injector gives us the opportunity to investigate two swirl numbers. By fixing the inner swirl number S_1, it is possible to study the effect of the outer swirl number and the momentum flux ratio as visualized in Fig. 9.

Figure 9 shows the evolution of NO_x emissions with respect to $J^{-\frac{1}{2}}$ for $S_1 = 0.87$, $\mathscr{P}_{th} = 10$ kW, three different values of S_2 and the flame types identified through OH* chemiluminescence images. The first trend that can be observed is that for $J^{-\frac{1}{2}} = 0.2$ to 0.5, NO_x emissions tend to increase with $J^{-\frac{1}{2}}$, regardless of the value of S_2. To understand this behavior, Fig. 10 shows the values of the chamber outlet temperature for the same conditions. Similarly, an increase in temperature with $J^{-\frac{1}{2}}$ can be observed and is attributed to the increase in equivalence ratio, as shown in Eq. 4 and Fig. 2. Higher temperatures within the chamber enhance NO_x formation through the thermal path.

Going back to Fig. 9, one can also note the stark decrease in NO_x emissions between type V and type IV flames for $S_2 = 0.7$ when $J^{-\frac{1}{2}}$ moves from 0.6 to 0.7. The reason behind this drop is clearly linked to the change in flame structure and was detailed in the previous section. Another remarkable feature in Fig. 9 is that a plateau appears to be reached for NO_x emissions in type I flames at $S_2 = 0.8$. This would suggest that emissions can become independent from $J^{-\frac{1}{2}}$ as its value gets closer to 1, at least in the case of type I flames. Finally, a decrease in NO_x emissions is observed at $S_2 = 0.6$ above $J^{-\frac{1}{2}} = 0.6$. This could be due to a progressive strengthening of the CRZ, akin to what is observed for $S_2 = 0.7$ and which causes a sudden variation in NO_x emissions between $J^{-\frac{1}{2}} = 0.6$ and 0.7. However, the progression in NO_x emissions appears to be more gradual in this particular case. We previously observed in Table 4 and

Fig. 8 a decrease in NO_x that could be linked with a strengthening of the CRZ causing the change in structure. In the present case, the gradual decrease in NO_x could be again linked to a progressive strengthening of the CRZ induced by the evolution of J, but this time not accompanied by a sudden change in structure. Complementary velocity measurements would be needed to assess this interpretation and are planned in future works.

Although structures tend to be dissimilar across values of S_2, it appears that flames stabilized using a stronger outer swirl level display lower NO_x emissions. When comparing two detached flames, this can be explained because higher swirl levels can enhance mixing between the fuel and the oxidizer to reduce the amount of high equivalence ratio hot spots in the flame and limit the amount of thermal NO_x in that way. However, most of the changes seem to be linked to a variation in flame structure induced by the modification of swirl, and not enough elements can highlight the effect of the swirl level itself for a given flame type.

Another factor that might play a role in the general increase in measured NO_x with $J^{-\frac{1}{2}}$ is the increased residence time induced by the reduction in oxidizer volume flow. Even though the real residence time depends on flow structures like recirculation zones whose effects cannot be measured with the current experimental apparatus, the estimate of residence time presented in Fig. 11 shows a twofold increase in residence time over the range of $J^{-\frac{1}{2}}$ explored. A lower residence time is observed for high S_2, high $J^{-\frac{1}{2}}$ flames due to lower densities linked to higher temperatures, but those do not seem to impact NO_x emissions significantly. Furthermore, the type I flames that emit the least NO_x in Fig. 9 also have the longest estimated residence time, thus reinforcing that flame structure is the more important factor in NO_x emissions.

Effect of the inner swirl number

Figure 12 shows the evolution of NO_x emissions when S_1 and J vary under fixed outer swirl number $S_2 = 0.7$ and thermal power $\mathscr{P}_{th} = 10$ kW. The associated exit temperatures are shown in Fig. 13 and appear to have little variation between different levels of inner swirl below $J^{-\frac{1}{2}} = 0.5$. It is interesting to note that this time, the flames with the highest level of swirl are not the ones that emit the least NO_x, as flames with $S_1 = 0.29$ emit less NO_x than flames with $S_1 = 0.87$. The likely reason behind this is the different flame structures. Indeed, the medium inner swirl value flames stabilize under an attached type I structure, whereas the high swirl flames stabilize under a type IV flame, or a type V detached flame for $J^{-\frac{1}{2}} < 0.6$. This can explain the difference in NO_x emissions and would suggest that detached flames tend to emit more NO_x than their attached counterpart. In turn, this could be due to the fact that attached flames burn under a diffusion flame regime, where the high shear forces at the injector lip could participate in reducing the flame temperature. This, however, does not explain why type I, $S_1 = 0$ flames emit the most NO_x in Fig. 12. While these flames qualify as type I since they possess an attached front flame at the injector lip, they feature a structure close to the jet visible in Fig. 6 that displays a quasi-total disappearance of the CRZ, which would entail a low level of shear and thus high flame temperature and high NO_x levels.

5 CONCLUSION

Non-premixed hydrogen flames were produced on a dual-swirl coaxial injector. Experiments varying the inner swirl number, outer swirl number and momentum flux ratio have shown that these parameters could easily influence flame structure. The various flame structures were divided in five categories based on different features of the flame front visualized through inverse Abel transformed OH* imagery. Attached, as well as lifted flames can be obtained. The evolution of the structure with the injection parameters has been described as well as the supposed interactions with the main flow structure, the CRZ. Then, we have shown that changes in structure can induce a great variation in nitrogen oxides emissions. The effect of a change in thermal power resulting in an effective scaling of the flow was also investigated, revealing a decrease in NO_x emissions that correlates with a reduced residence time within the chamber. Finally, the global evolution of NO_x emissions following the different parameters has been exposed, showing a link with exit temperature as well as an effect of swirl number beyond the induced changes in flame structure. These various elements show that the coaxial swirl injector allows the control of many parameters in the flame, namely structure, and the flow itself, which affects residence time and temperature. All these aspects are essential in controlling NO_x emissions.

This work opens up new perspectives for future experiments. Additional diagnostics like Particle Image Velocimetry are envisioned to gather detailed knowledge of the flow field and its evolution with the injection parameters, to better understand the mechanism behind structure changes and flame liftoff. Simulations can also be employed to yield a complementary analysis and explore the mechanism of NO_x formation within the flame. The experimental setup can also be modified to approach more realistic conditions within a gas turbine combustion chamber, such as reduced residence time, lower heat losses yielding higher exit temperature and higher pressures, which are all factors that can strongly affect NO_x emissions.

REFERENCES

[1] Chen, T.-M., Kuschner, W. G., Gokhale, J., and Shofer, S., 2007. "Outdoor Air Pollution: Nitrogen Dioxide, Sulfur Dioxide, and Carbon Monoxide Health Effects". *Am. J. Med. Sci.,* ***333***(4), 4, pp. 249–256.

[2] Johnson, C., Henshaw, J., and Mclnnes, G., 1992. "Impact of aircraft and surface emissions of nitrogen oxides on tropospheric ozone and global warming". *Nature,* ***355***(6355), 1, pp. 69–71.

[3] Skottene, M., and Rian, K. E., 2007. "A study of NOx formation in hydrogen flames". *Int. J. Hydrog. Energy,* ***32***(15), 10, pp. 3572–3585.

[4] Lhuillier, C., Oddos, R., Zander, L., Lückoff, F., Göckeler, K., Paschereit, C. O., and Djordjevic, N., 2017. "Hydrogen-Enriched Methane Combustion Diluted With Exhaust Gas and Steam: Fundamental Investigation on Laminar Flames and NOx Emissions". In Proceedings of the ASME Turbo Expo 2017, ASME. GT2017-64885.

[5] Göke, S., Schimek, S., Terhaar, S., Reichel, T., Göckeler, K., Krüger, O., Fleck, J., Griebel, P., and Oliver Paschereit, C., 2014. "Influence of Pressure and Steam Dilution on NOx and CO Emissions in a Premixed Natural Gas Flame". *ASME J. Eng. Gas*

Turbines Power, ***136***(9), 9, p. 091508.

[6] Ingenito, A., Agresta, A., Andriani, R., and Gamma, F., 2015. "RQL Combustion as an Effective Strategy to NOx Reduction in Gas Turbine Engines". In Proceedings of the ASME 2014 International Mechanical Engineering Congress and Exposition, Vol. 1: Advances in Aerospace Technology, ASME. IMECE2014-36898.

[7] Bothien, M. R., Ciani, A., Wood, J. P., and Fruechtel, G., 2019. "Toward Decarbonized Power Generation With Gas Turbines by Using Sequential Combustion for Burning Hydrogen". *ASME J. Eng. Gas Turbines Power,* ***141***(12), 11.

[8] Cappelletti, A., and Martelli, F., 2017. "Investigation of a pure hydrogen fueled gas turbine burner". *Int. J. Hydrog. Energy,* ***42***(15), 4, pp. 10513–10523.

[9] Funke, H. H.-W., Beckmann, N., Keinz, J., and Horikawa, A., 2021. "30 Years of Dry-Low-NOx Micromix Combustor Research for Hydrogen-Rich Fuels—An Overview of Past and Present Activities". *ASME J. Eng. Gas Turbines Power,* ***143***(7), 3.

[10] Boyd Fackler, K., Karalus, M., Novosselov, I., Kramlich, J., Malte, P., and Vijlee, S., 2015. "NOx Behavior for Lean-Premixed Combustion of Alternative Gaseous Fuels". *ASME J. Eng. Gas Turbines Power,* ***138***(4), 10. 041504.

[11] Cheng, R. K., Littlejohn, D., Strakey, P. A., and Sidwell, T., 2009. "Laboratory investigations of a low-swirl injector with H2 and CH4 at gas turbine conditions". *Proc. Combust. Inst,* ***32***(2), 1, pp. 3001–3009.

[12] Lin, Y.-C., Daniele, S., Jansohn, P., and Boulouchos, K., 2012. "Combustion Characteristics and NOX Emission of Hydrogen-Rich Fuel Gases at Gas Turbine Relevant Conditions". In Proceedings of the ASME Turbo Expo 2012, ASME, pp. 829–835. GT2012-69080.

[13] Reichel, T. G., and Paschereit, C. O., 2017. "Interaction mechanisms of fuel momentum with flashback limits in lean-premixed combustion of hydrogen". *Int. J. Hydrog. Energy,* ***42***(7), 2, pp. 4518–4529.

[14] Reichel, T. G., Terhaar, S., and Paschereit, O., 2015. "Increasing Flashback Resistance in Lean Premixed Swirl-Stabilized Hydrogen Combustion by Axial Air Injection". *ASME J. Eng. Gas Turbines Power,* ***137***(7), 7.

[15] Mira, D., Lehmkuhl, O., Both, A., Stathopoulos, P., Tanneberger, T., Reichel, T. G., Paschereit, C. O., Vázquez, M., and Houzeaux, G., 2020. "Numerical Characterization of a Premixed Hydrogen Flame Under Conditions Close to Flashback". *Flow Turbul. Combust.,* ***104***(2), 3, pp. 479–507.

[16] Feikema, D., Chen, R.-H., and Driscoll, J. F., 1990. "Enhancement of flame blowout limits by the use of swirl". *Combust. Flame,* ***80***(2), 5, pp. 183–195.

[17] Yuasa, S., 1986. "Effects of swirl on the stability of jet diffusion flames". *Combust. Flame,* ***66***(2), 11, pp. 181–192.

[18] Syred, N., Chigier, N. A., and Beér, J. M., 1971. "Flame stabilization in recirculation zones of jets with swirl". *Symp. (Int.) Combust.,* ***13***(1), 1, pp. 617–624.

[19] Terasaki, T., and Hayashi, S., 1996. "The effects of fuel-air mixing on NOx formation in non-premixed swirl burners". *Symp. (Int.) Combust.,* ***26***(2), 1, pp. 2733–2739.

[20] Claypole, T. C., and Syred, N., 1981. "The effect of swirl burner aerodynamics on NOx formation". *Symp. (Int.) Combust.,* ***18***(1), 1, pp. 81–89.

[21] Degenève, A., Mirat, C., Caudal, J., Vicquelin, R., and Schuller, T., 2019. "Effects of Swirl on the Stabilization of Non-Premixed Oxygen-Enriched Flames Above Coaxial Injectors". *ASME J. Eng. Gas Turbines Power,* ***141***(12), 12, p. 121018.

[22] Degenève, A., Vicquelin, R., Mirat, C., Caudal, J., and Schuller, T., 2021. "Impact of co- and counter-swirl on flow recirculation and liftoff of non-premixed oxy-flames above coaxial injectors". *Proc. Combust. Inst,* ***38***(4), 1, pp. 5501–5508.

[23] Merlo, N., Boushaki, T., Chauveau, C., Persis, S. D., Pillier, L., Sarh, B., and Gökalp, I., 2014. "Combustion characteristics of methane–oxygen enhanced air turbulent non-premixed swirling flames". *Exp. Therm. Fluid Sci.,* ***56***, 7, pp. 53–60.

[24] Brohez, S., Delvosalle, C., and Marlair, G., 2004. "A two-thermocouples probe for radiation corrections of measured temperatures in compartment fires". *Fire Saf. J.,* ***39***(5), 7, pp. 399–411.

[25] Gupta, A. K., Lilley, D. G., and Syred, N., 1984. *Swirl flows*. Energy and engineering science series. Abacus Press, Tunbridge Wells, Kent.

[26] Baukal, C., and Eleazer, P., 1998. "Quantifying NO $_{\mathrm{X}}$ for Industrial Combustion Processes". *J. Air Waste Manag. Assoc.,* ***48***(1), 1, pp. 52–58.

[27] Schefer, R. W., Kulatilaka, W. D., Patterson, B. D., and Settersten, T. B., 2009. "Visible emission of hydrogen flames". *Combust. Flame,* ***156***(6), 6, pp. 1234–1241.

[28] Vu, B. T., and Gouldin, F. C., 1982. "Flow Measurements in a Model Swirl Combustor". *AIAA J.,* ***20***(5), 5, pp. 642–651.

[29] Chen, R.-H., Driscoll, J. F., Kelly, J., Namazian, M., and Schefer, R. W., 1990. "A Comparison of Bluff-Body and Swirl-Stabilized Flames". *Combust. Sci. Technol.,* ***71***(4-6), 6, pp. 197–217.

TABLE 1. Parameter values

Parameter	Range	Parameter	Range
S_1 [-]	0,0.29,0.87	S_2 [-]	0.6,0.7,0.8
$J^{-\frac{1}{2}}$ [-]	0.2-0.9	Φ [-]	0.19-0.87
Re_1 [-]	2000	U_1 [m·s^{-1}]	35
Re_2 [-]	7000-30000	U_2 [m·s^{-1}]	11-47
$\mathscr{P}_{th}$ [kW]	10	Pressure [atm]	1

TABLE 2. Gas analyzer specifications

Species [unit]	Range	Repeatability	Sensitivity
NO [ppmvd]	0-500	$\pm$ 2.5	0.1
O_2 [vol% d]	0-21	$\pm$ 0.105	0.01

TABLE 3. NO_x emissions evolution with flame thermal power. Injection parameters: $J^{-\frac{1}{2}} = 0.5$, $\Phi = 0.49$, $S_1 = 0.87$, $S_2 = 0.8$, $\mathscr{P}_{th} = 10$ kW

$\mathscr{P}_{th}$ [kW]	5	7.5	10	15
NO_x @ 15% O_2 [ppmvd]	15.9	13.6	11.7	10.5
T_{exit} [K]	807	883	950	1034
$\tau_{res}[s]$	0.72	0.44	0.31	0.19

TABLE 4. NO_x emissions and chamber exit temperature at $J^{-\frac{1}{2}} = 0.6$, $\Phi = 0.58$, $S_1 = 0.87$, $S_2 = 0.7$ and $\mathscr{P}_{th} = 10$ kW by flame type

TYPE	IV	V
NO_x @ 15% O_2 [ppmvd]	18.4	23.3
T_{exit} [K]	989	1080

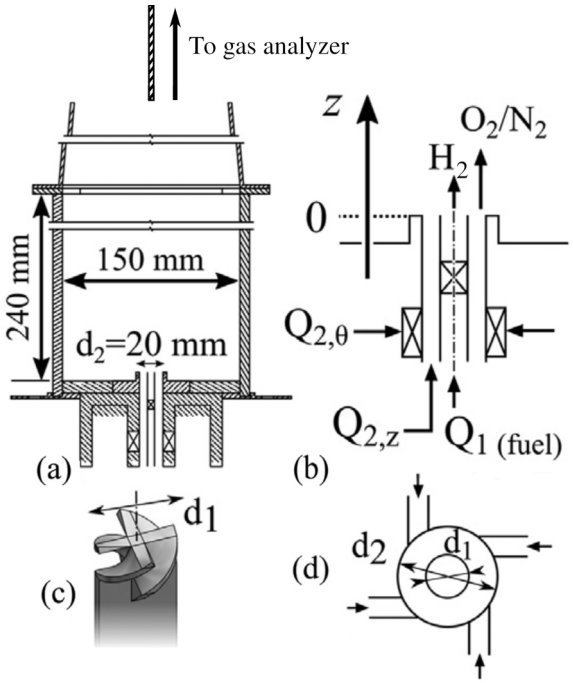

FIGURE 1. (a) Diagram of the combustion chamber (b) Coaxial injector longitudinal cut (c) Swirl vane model (d) Injector transverse cut. (Adapted from [22])

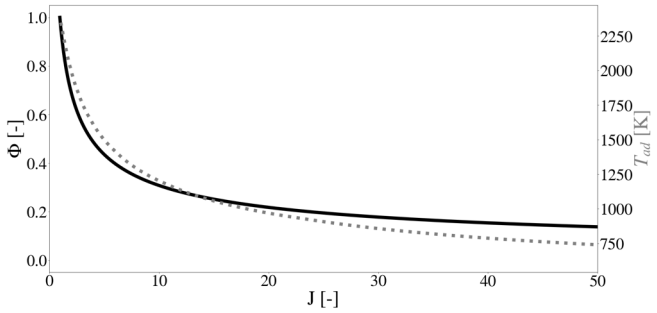

FIGURE 2. Equivalence ratio Φ and associated adiabatic flame temperature as a function of momentum flux ratio J. Solid: Global equivalence ratio. Dotted : Adiabatic flame temperature

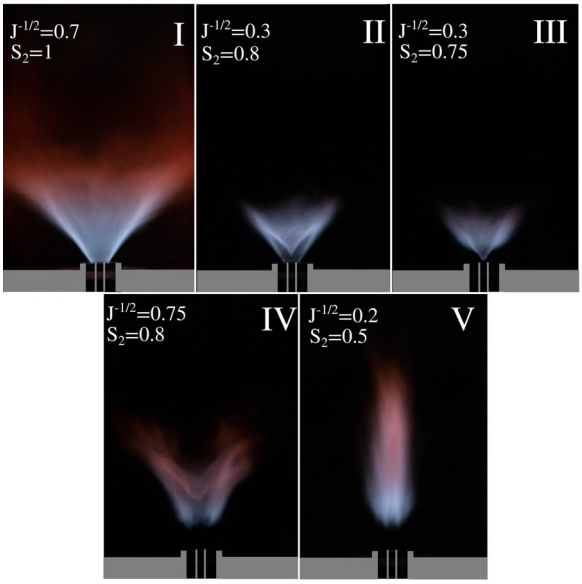

FIGURE 3. Short exposure time visible range image of the different flame types. $\mathscr{P}_{th} = 10$ kW, $S_1 = 0.87$.Credit: Cécile Oriot - CentraleSupélec.

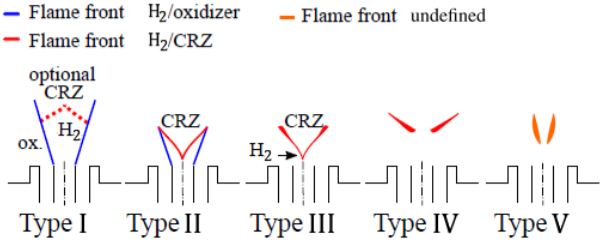

FIGURE 4. Flame structure types observed on the dual-swirl coaxial injector. Adapted from [21]

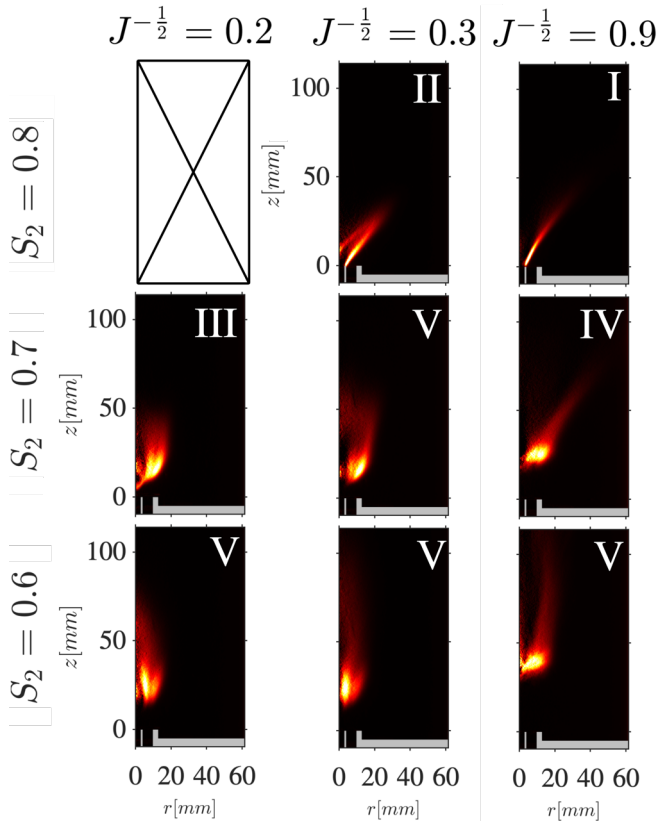

FIGURE 5. Hydrogen flames observed by OH* chemiluminescence (Inverse Abel transformed) for different J and S_2 conditions and fixed $S_1 = 0.87$, $\mathscr{P}_{th} = 10$ kW

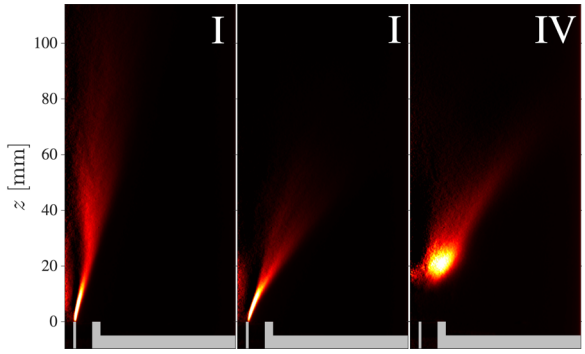

FIGURE 6. Inverse Abel transformed OH* images of flames with $J^{-\frac{1}{2}} = 0.7$, $S_2 = 0.7$, and $\mathscr{P}_{th} = 10$ kW. Left to right: $S_1 = 0$; $S_1 = 0.29$; $S_1 = 0.87$

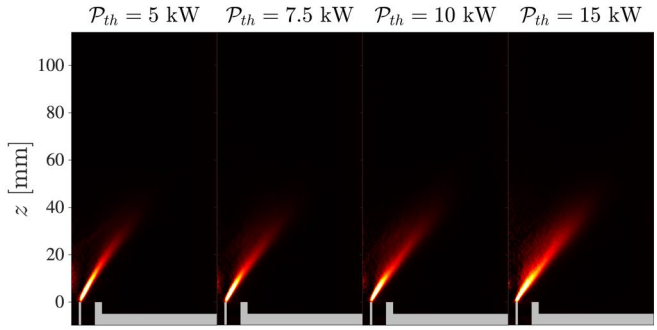

FIGURE 7. Inverse Abel transformed OH* chemiluminescence flame structure as a function of thermal power. Injection parameters: $J^{-\frac{1}{2}} = 0.5$, $\Phi = 0.49$, $S_1 = 0.87$, $S_2 = 0.8$

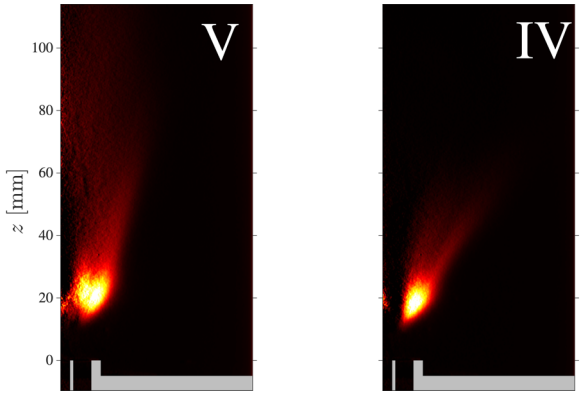

FIGURE 8. Inverse Abel transform of OH* chemiluminescence for two flame types possible at injection parameters : $J^{-\frac{1}{2}} = 0.6$, $\Phi = 0.58$, $S_1 = 0.87$, $S_2 = 0.7$, $\mathscr{P}_{th} = 10$ kW

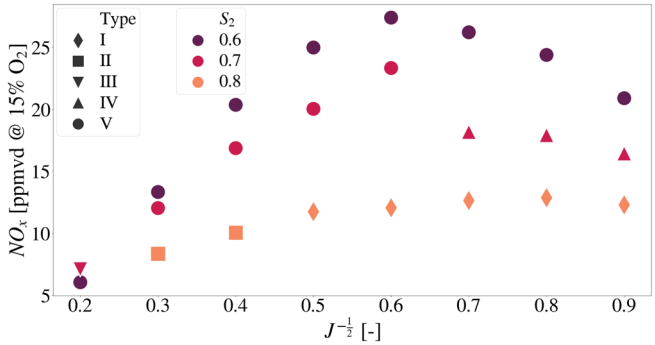

FIGURE 9. Corrected NO_x as a function of $J^{-\frac{1}{2}}$ and S_2, $S_1 = 0.87$, $\mathscr{P}_{th} = 10$ kW

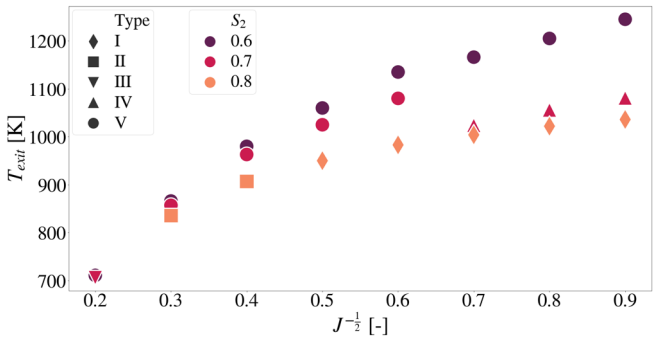

FIGURE 10. Chamber exit temperature as a function of $J^{-\frac{1}{2}}$ and S_2, $S_1 = 0.87$, $\mathscr{P}_{th} = 10$ kW

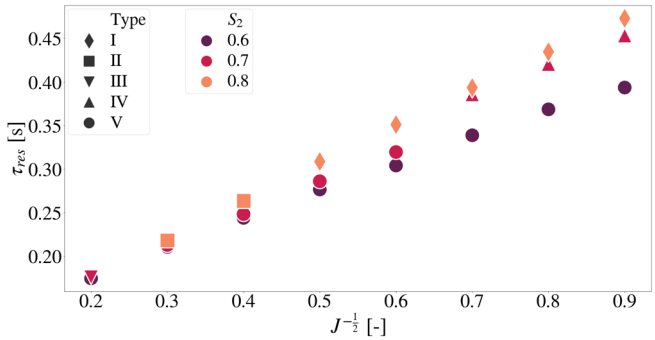

FIGURE 11. Estimated residence time as a function of $J^{-\frac{1}{2}}$ and S_2, $S_1 = 0.87$, $\mathscr{P}_{th} = 10$ kW

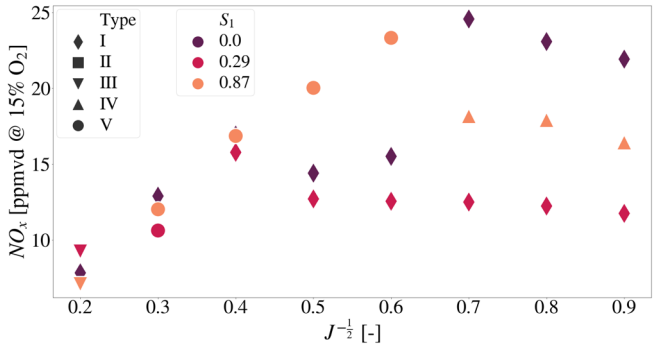

FIGURE 12. Corrected NO_x as a function of $J^{-\frac{1}{2}}$ and S_1, $S_2 = 0.7$, $\mathscr{P}_{th} = 10$ kW

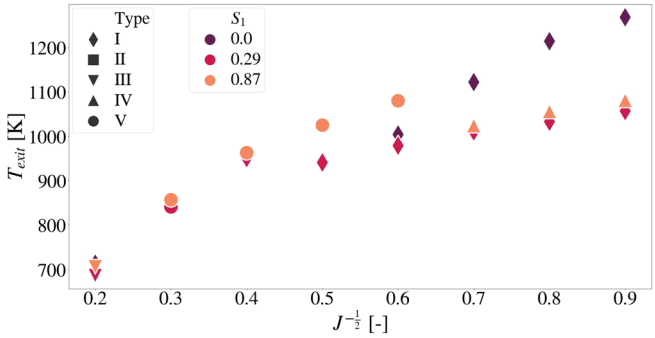

FIGURE 13. Chamber exit temperature as a function of $J^{-\frac{1}{2}}$ and S_1, $S_2 = 0.7$, $\mathscr{P}_{th} = 10$ kW